Nanoscale

PAPER

View Article Online
View Journal | View Issue

Cite this: *Nanoscale*, 2024, **16**, 11592

A suitably fabricated ternary nanocomposite (Cu-CuO@rGO-SiO_2) as a sustainable and common heterogeneous catalyst for C–S, C–O and C–N coupling reactions†

Prasun Choudhury, [a] Sujit Ghosh,[b] Kinkar Biswas*[a] and Basudeb Basu *[c]

Received 15th March 2024,
Accepted 24th May 2024

DOI: 10.1039/d4nr01116c

rsc.li/nanoscale

A hybrid composite based on π-electron rich reduced graphene oxide (rGO) and mesoporous silica (SiO_2) was prepared and decorated with copper species to afford a ternary nanocomposite material (Cu-CuO@rGO-SiO_2). This copper-based nanocomposite was successfully used as a robust and multi-tasking heterogeneous catalyst for most common cross-coupling reactions (*e.g.* C–S, C–O and C–N coupling). A broad range of catalytic activities are believed to be originated from the synergism of different co-existing copper species (Cu(0) and CuO) and facile charge transfer from the metal ions towards rGO–SiO_2 matrices, as established from XPS and other studies.

Introduction

The role of transition metals in various cross-coupling reactions has been well established over the last few decades.[1–3] Among the various transition metals, palladium is the most prevalent one in various cross-coupling and C–H bond activation reactions.[4–6] Numerous solid-supported Pd-catalysts,[7,8] bimetallic Cu/Pd nanoclusters,[9] and photocatalysts[10,11] have been effectively synthesized and used in S–S coupling,[12,13] C–C coupling,[14] and other organic transformations. But copper catalyzed cross-coupling reactions have attracted immense attention over palladium catalysts due to their easy accessibility, low cost and low toxicity.[15–18] Another significant feature of copper catalysis is the catalytic selectivity, which significantly depends on the type of copper species actually involved. For instance, metallic copper and various copper oxide phases play an imperative role in catalyzing specific organic transformations.[19–26] Moreover, the presence of copper species in the form of Cu_2O–CuO/Cu, Cu_2O–CuO and Cu–Cu_2O–CuO leads to distinctive catalytic activity.[27–32] Furthermore, their catalytic activity could be improved if they are immobilized on suitable materials having a high surface area. These include mesoporous and microporous materials like silica, zeolites, metal-organic frameworks (MOFs), *etc.*[33–36] Recently, the use of carbonaceous nanomaterials as a solid support has emerged in heterogeneous catalysis, presumably due to their robustness, enhanced stability and higher surface area.[37]

Although a large variety of homogeneous and heterogeneous metal catalysts have been developed and employed in diverse cross-coupling reactions ranging from C–C to C–X (X = N, O, S, P *etc.*) couplings with varying successes, it is evident at this stage that a single catalytic system, which is able to catalyze all types of cross couplings, would be of primary importance. The catalytic system should be easily and cheaply obtainable, robust, and eco-friendly with a high TOF and recyclability. No such catalytic system has ever been developed except for some sporadic attempts and/or success with some types of couplings. We address this issue with a judicious choice of supports as well as metallic species so as to obtain a wide-ranging but robust catalytic system.

Graphene oxide (GO), a two-dimensional honeycomb lattice with a flat mono- or few-layer structure, has attracted enormous attention in the field of organic synthesis.[38] Due to the presence of multiple oxygenated moieties coupled with a large surface area, GO has been used to prepare several functional materials for adsorption, catalysis, sensors, electronics and optics.[39,40] Moreover, metal/graphene oxide composites play a crucial role in catalysis, fabrication of sensors, toxic metal ion scavenging, cellular imaging and drug delivery.[41–43] Graphene supported metal/metal oxide catalysts however have certain limitations. Graphene sheets usually tend to aggregate due to the strong π–π stacking interactions between the individual graphene layers which might block the active catalytic sites

[a]*Department of Chemistry, University of North Bengal, Darjeeling 734013, India. E-mail: kinkar.chem@nbu.ac.in*
[b]*Raiganj Surendranath Mahavidyalaya, Raiganj, Uttar Dinajpur 733134, India*
[c]*Formerly Department of Chemistry, University of North Bengal, Darjeeling 734013, India. E-mail: basudeb.basu@gmail.com*

†Electronic supplementary information (ESI) available: Experimental details, characterization data, and ^1H and ^{13}C NMR spectra of isolated compounds. See DOI: https://doi.org/10.1039/d4nr01116c

and disrupt the overall catalytic function.[44] Moreover, due to the high surface energy as well as harsh reaction conditions employed during catalytic reactions, metal nanoparticles become unstable and agglomerate into larger species resulting in a significant drop in the overall catalytic performance.[45] To avoid the agglomeration of metal species and subsequent low catalytic performance, we envisioned that graphene oxide should be functionalized in such a way so that the stability of metal-supported graphene improves and the π–π stacking interactions between individual layers can be restrained.

Silica-based mesoporous materials have been widely used in diverse fields including catalysis owing to its thermal and chemical stability, low toxicity and easy functionalizations.[46] We presumed that the combination of these two materials to form a silica/graphene oxide hybrid composite might prevent the aggregation of metal species. Furthermore, the hybrid material could exhibit superior physical and chemical properties like thermal stability and catalytic performance due to their synergistic effects.[47] Since silica-based meso-structured catalysts are mainly utilized in liquid phase reactions, covalent bonding between the active species and the support surface is favored in order to minimize the undesired sintering and leaching of the anchored groups and metal species through the nanoconfinement effect.[48]

The reducibility of graphene oxide-silica (GO-SiO_2) has been retarded by introducing silica groups onto the GO surface. During the preparation of the GO-SiO_2 nanocomposite, tetraethyl orthosilicate (TEOS) has been hydrolyzed and attached on the graphene oxide surface. The introduction of –OH groups on the surface of GO-SiO_2 makes it more dispersible in polar protic solvents. Herein we report the synthesis of a copper-copper oxide immobilized graphene oxide-silica nanocomposite (Scheme 1). This new ternary nanocomposite, designated as Cu-CuO@rGO-SiO_2, has been characterized by several spectroscopic and electron microscopic techniques and finally used as a versatile, multi-tasking catalyst in different C–heteroatom cross-coupling reactions.

Results and discussion

As a part of our growing interest in graphene-based nanomaterials for catalysis,[49] we sought to synthesize a well-designed and novel ternary nanocomposite (Cu-CuO@rGO-SiO_2) and explore its catalytic activity in various carbon–heteroatom (–N, –O, –S, *etc.*) coupling reactions. The functionalization of graphene oxide with silica was effectively carried out by the hydrolysis of tetraethyl orthosilicate (TEOS) in a suspension of hydrophilic GO.[50] The synthesized graphene oxide-silica (GO-SiO_2) composite was used as a heterogeneous support for immobilization of copper-copper oxide species. The ternary nanocomposite was characterized in detail by various spectroscopic and microscopic techniques such as Fourier transform infrared spectroscopy (FT-IR), Raman spectroscopy, X-ray photoelectron spectroscopy (XPS), scanning electron microscopy/energy dispersive spectroscopy (SEM-EDS), high-resolution transmission electron microscopy (HRTEM) and powder X-ray diffraction (PXRD).

The FT-IR spectra of the as-synthesized GO, GO-SiO_2 and Cu-CuO@rGO-SiO_2 were recorded (Fig. 1). The peaks at 3423 and 1397 cm^{-1} for GO were attributed to the stretching and deformation of –OH groups, respectively.[51] The band centered at 1046 cm^{-1} is associated with the stretching of the C–O bond, while the stretching vibration of the C=O groups in GO was noted at 1721 cm^{-1}.[51] GO on treatment with TEOS afforded the GO-SiO_2 hybrid that exhibited characteristic sharp

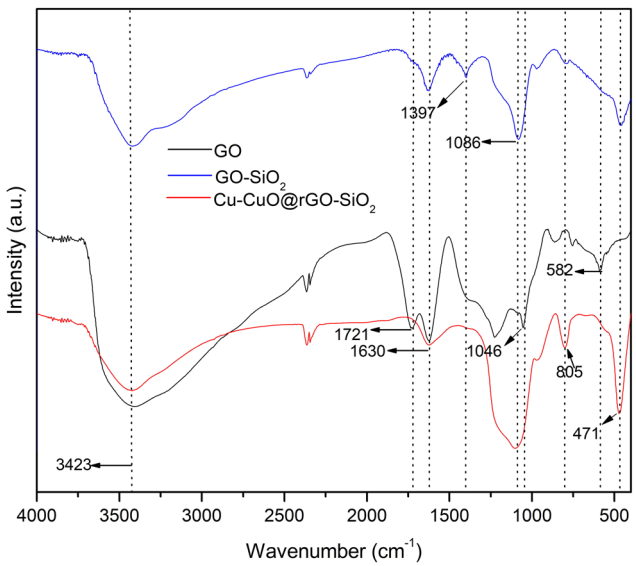

Fig. 1 FT-IR spectra of GO, GO-SiO_2 and Cu-CuO@rGO-SiO_2.

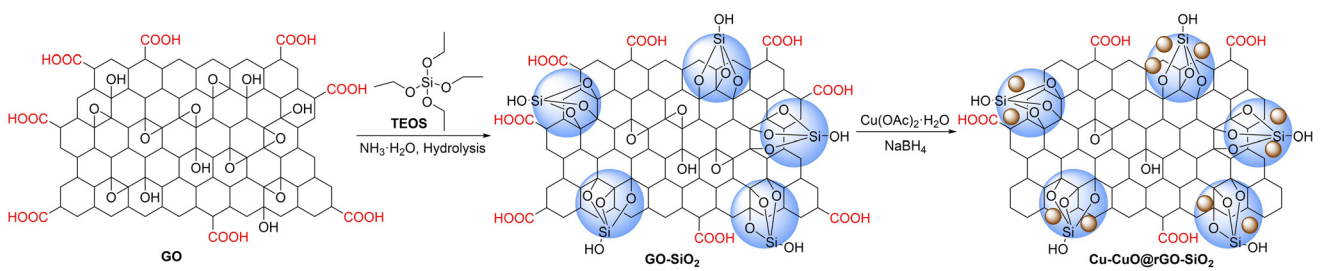

Scheme 1 Schematic representation of the synthesis of the Cu-CuO@rGO-SiO_2 nanocomposite.

peaks at 471 and 805 cm^{-1} owing to the Si–O–Si bending (wagging) and stretching vibration of silica, while the absorption band at 1086 cm^{-1} could be from the symmetric stretching vibration of the Si–O bond of Si–O–Si or O–Si–O frameworks.[52] The typical carbonyl group band of GO at 1721 cm^{-1} disappeared indicating the conversion of C═O groups to Si–O–C bonds.[53] The broad absorption band in the region 3400–3500 cm^{-1} clearly demonstrates the presence of –OH groups in GO-SiO_2 (as C–OH and Si–OH). In the FT-IR spectrum of the Cu-CuO@rGO-SiO_2 nanocomposite, the intensity of –OH stretching was reduced significantly indicating the reduction of GO to rGO during the grafting process of the metal onto the GO-SiO_2 surface. In the comparative FT-IR spectra of GO, GO-SiO_2 and Cu-CuO@rGO-SiO_2, the characteristic peaks between 1300 and 1600 cm^{-1} were absent in the spectrum of the Cu-CuO@rGO-SiO_2 nanocomposite indicating the detachment of the oxygen-containing groups.[54]

The powder X-ray diffraction (PXRD) patterns of the GO-SiO_2 hybrid and the Cu-CuO@rGO-SiO_2 nanocomposite are given in Fig. 2. The GO-SiO_2 hybrid shows two sharp diffraction peaks at 10.65° and 42.49° which originate from the graphene oxide (GO) plates.[42] Moreover, a broad peak at 23.24° was due to the leading effect of silica particles in the hybrid composite.[50] The XRD patterns of the Cu-CuO@rGO-SiO_2 nanocomposite showed the diffraction peaks at $2\theta \sim 36.5°$ (111), 74.0° (311) and 77.9° (222) which were attributed to the presence of CuO species (JCPDS# 01-078-0428). Moreover, the diffraction peaks at $2\theta \sim$ 43.4° (111) and 50.5° (200) indicate the presence of Cu(0) species (JCPDS# 01-071-4609). The disappearance of the characteristic diffraction peak at 10.65° in Cu-CuO@rGO-SiO_2 suggested the conversion of GO-SiO_2 to rGO-SiO_2.

The characteristic D- and G- bands of GO, GO-SiO_2 and Cu-CuO@rGO-SiO_2 have been observed in the Raman spectra (Fig. 3). The higher intensity of the G-band (I_G) than that of the D-band (I_D) has been observed for GO. However, the intensity of the D-bands increased in GO-SiO_2 and Cu-CuO@rGO-SiO_2 ($I_D/I_G > 1$). Such observations indicated the conversion of GO to rGO and the successful incorporation of copper species in the nanocomposite.[49]

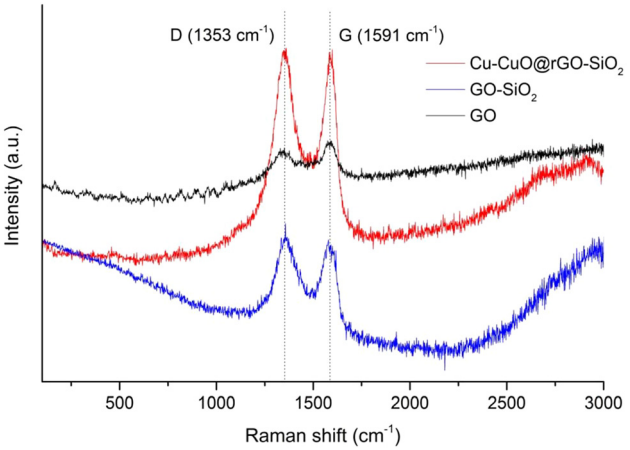

Fig. 3 Raman spectra of GO, GO-SiO_2 and Cu-CuO@rGO-SiO_2.

The characteristic layered structure of GO obtained by sonication and the successful decoration of silica nanoparticles on the layered GO surface by hydrolysis of TEOS in the GO-SiO_2 composite were affirmed from SEM images. The doping of copper species on the GO-SiO_2 composite was also confirmed from SEM images (Fig. 4). The stacking nature of graphite flakes and the exfoliated GO layers are shown in Fig. 4a and b respectively. The distribution of silica nanoparticles on the surface of GO is shown in Fig. 4c and the immobilization of copper species on the nanocomposite (Cu-CuO@rGO-SiO_2; since GO-SiO_2 was reduced to rGO-SiO_2 during the synthesis procedure) surface is revealed in Fig. 4d. The enlarged view in the inset of Fig. 4d shows the deposition of copper species on the surface of rGO-SiO_2 in a uniform manner. The SEM-energy dispersive X-ray spectroscopy (SEM-EDS) of Cu-CuO@rGO-SiO_2 established the presence of Cu along with other elements C, O and Si (originated from rGO-SiO_2) in the ternary nanocomposite (Fig. 5).

The size and shape of Cu-CuO@rGO-SiO_2 were analyzed from high resolution transmission electron microscopy (Fig. 6). Fig. 6a represents the distribution of nanosized Cu(0) and CuO nanoparticles on the rGO-SiO_2 surface. The TEM images show fairly uniform distributions of Cu(0) and CuO nanoparticles in the range ~5–15 nm on the nanocomposite matrices (inset of Fig. 6b). The significant structural detail of Cu-CuO@rGO-SiO_2 has been revealed by high-resolution TEM (Fig. 6c). The well-defined silica region and rGO layers were clearly observed indicating the uniform distribution of copper species on the silica surface without any aggregation.[55] The deposition of Cu(0) and CuO on the rGO-SiO_2 surface was clearly observed in HRTEM at 5 nm magnification (Fig. 6d). The insets of Fig. 6d revealed the selected area electron diffraction (SAED) patterns and magnified view of the lattice fringes of Cu(0) and CuO species.

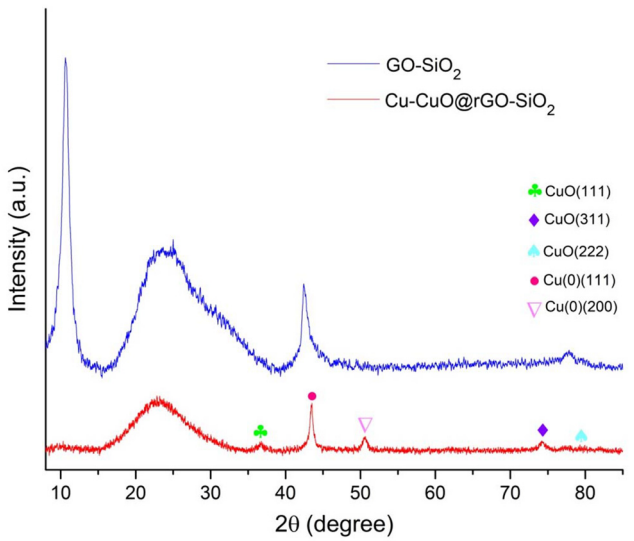

Fig. 2 XRD patterns of GO-SiO_2 and Cu-CuO@rGO-SiO_2.

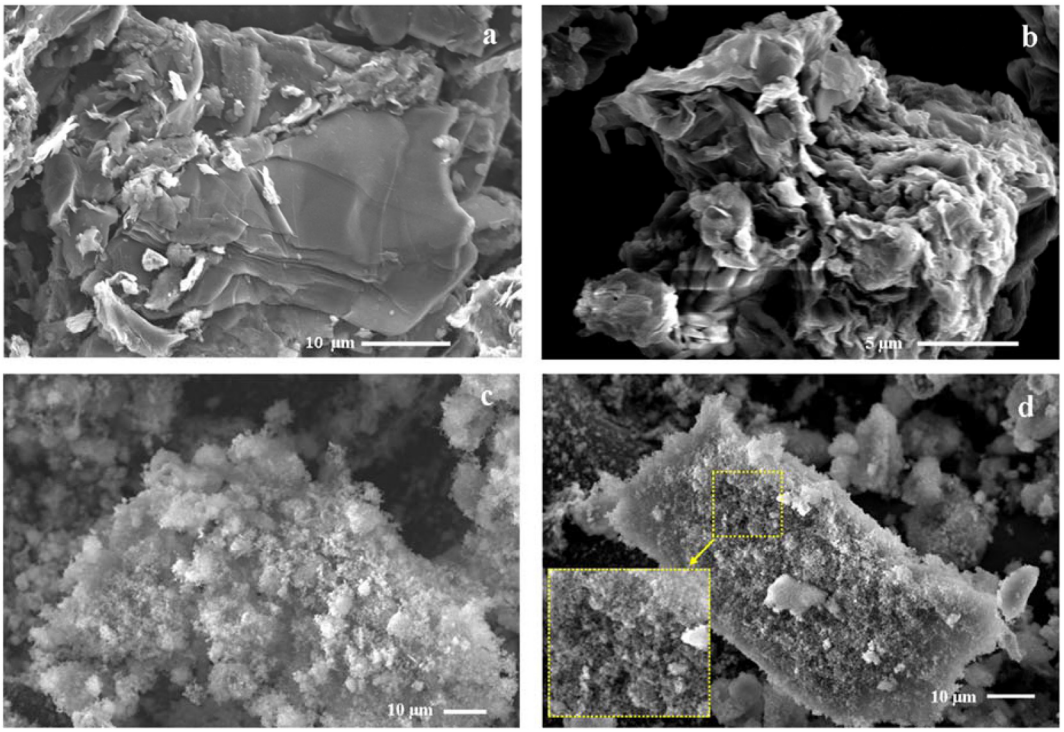

Fig. 4 SEM images of (a) graphite, (b) graphene oxide, (c) the GO-SiO_2 hybrid, and (d) Cu-CuO@rGO-SiO_2.

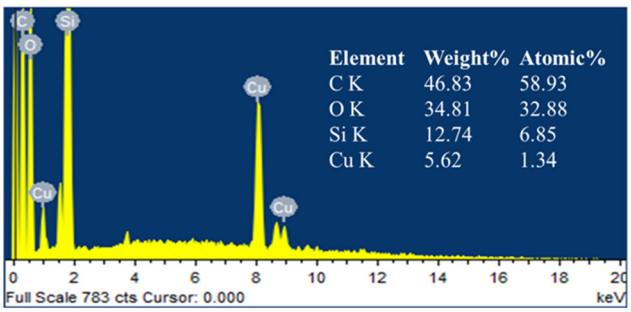

Fig. 5 SEM-EDS image of Cu-CuO@rGO-SiO_2.

The X-ray photoelectron spectroscopy (XPS) was performed to investigate the elemental composition and chemical state of the components present on the surface of the catalyst (Cu-CuO@rGO-SiO_2). The XPS survey spectra of the nanocomposite showed binding energy peaks of Cu 2p, O 1s, C 1s and Si 2p, indicating the successful incorporation of copper species into the surface of the nanocomposite (Fig. 7). For detailed analysis regarding the interaction between Cu, rGO and SiO_2, the deconvolution of C 1s, O 1s and Cu 2p was performed. The deconvoluted C 1s spectrum showed a binding energy peak at 284.4 eV (C═C) arising from the sp^2 domain of rGO.[48] In addition, the peaks at 285.4, 286.6, 287.7 and 289.0 eV were attributed to the presence of C–OH, C–O–C, C═O and O═C–O functional groups on rGO, respectively (Fig. 7b).[49] The high-resolution O 1s spectrum is composed of three prominent peaks in the region of 531.5–535.1 eV (Fig. 7c). The binding energy values 531.5 and 532.6 eV were due to O═C–O and C═O functional groups on rGO. The significant peak at 535.1 eV could be either due to C–OH or C–O–Si groups.[56] The deconvoluted XPS core spectra representing Cu $2p_{3/2}$ and Cu $2p_{1/2}$ regions are illustrated in Fig. 7d. The appearance of characteristic binding energy peaks at 934.2 and 954.2 eV indicated the presence of Cu(0) species (Cu $2p_{3/2}$ and Cu $2p_{1/2}$ respectively) in the nanocomposite.[48] The binding energy peaks at 936.2 and 955.8 eV respectively in the deconvoluted Cu $2p_{3/2}$ and Cu $2p_{1/2}$ XPS spectra specified the presence of the Cu^{2+} oxidation state.[48] Additionally, the shakeup satellite peaks with binding energies at ~944.2 eV (Cu $2p_{3/2}$) and ~964.1 eV (Cu $2p_{1/2}$) indicated the existence of the Cu–O bond in CuO species.[48] These results indicate that both Cu(0) and CuO species coexist on the surface of the rGO-SiO_2 composite. Furthermore, the binding energy shift of the Cu $2p_{3/2}$ core level (936.2 eV) has been assigned due to the charge transfer from the metal ions towards the rGO-SiO_2 matrix.[57] The co-existence and charge transfer towards the hybrid matrices might result in synergistic interactions between different copper species and the rGO-SiO_2 composite.

The specific surface area, pore size and pore volume were studied by gas adsorption measurements on the Cu-CuO@rGO-SiO_2 nanocomposite using N_2 at 77 K. The specific surface area of the nanocomposite was calculated from the isotherm using the Brunauer–Emmett–Teller (BET) method and found to be 193 $m^2\ g^{-1}$ (Fig. 8). The size of the pores and the pore volume were calculated as 3.4 nm and 0.67 $cm^3\ g^{-1}$ respectively. The surface area observed for the nanocomposite

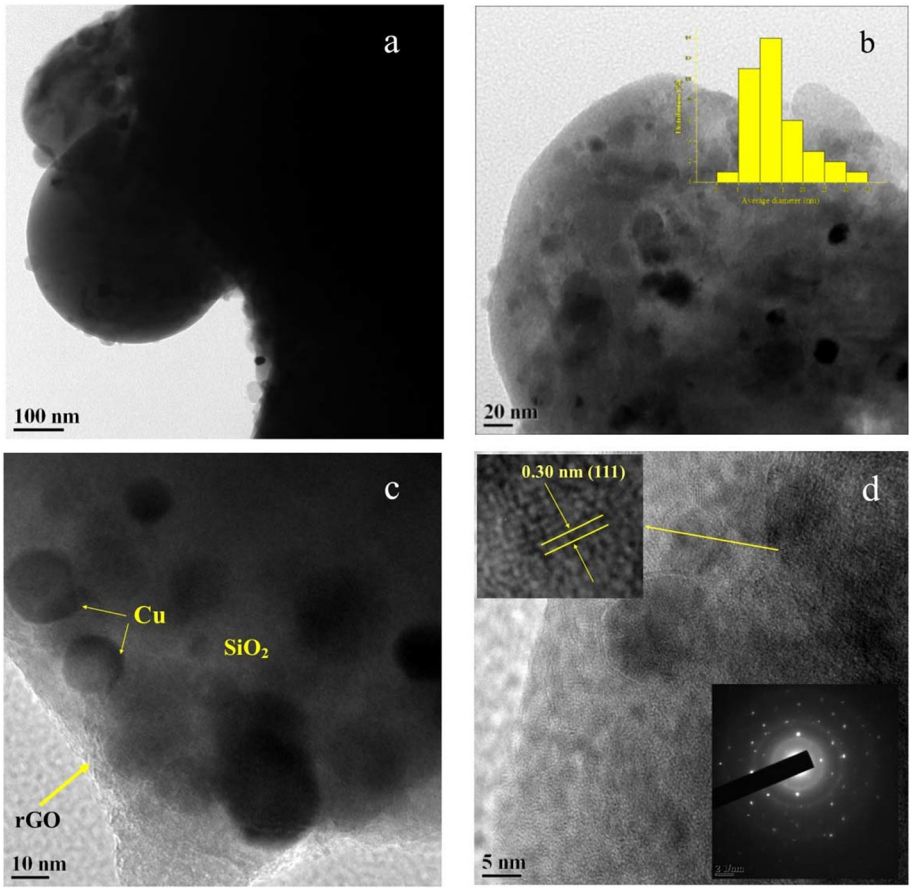

Fig. 6 HRTEM images of Cu-CuO@rGO-SiO_2 (a–c) and SAED patterns (d).

indicates that rGO-SiO_2 could be an excellent support for the immobilization of Cu–CuO species.[58]

Finally, the presence of copper in the ternary nanocomposite was measured by inductively coupled plasma mass spectrometry (ICP-MS). For this purpose, the nanocomposite catalyst (3.3 mg) was digested with super pure nitric acid (5 mL) and the copper content was estimated to be 1.026 mmol g^{-1} of the Cu-CuO@rGO-SiO_2 nanocomposite.

Catalytic activity of the Cu-CuO@rGO-SiO_2 nanocomposite

The as-prepared Cu-CuO@rGO-SiO_2 nanocomposite was used to evaluate its catalytic activity for various (C–S, C–O and C–N) cross-coupling reactions.

Cu-CuO@rGO-SiO_2 nanocomposite catalyzed C–S cross-coupling reaction

The C–S cross-coupling reaction was investigated in the presence of the Cu-CuO@rGO-SiO_2 nanocomposite using 4-iodoanisole and thiophenol as the model substrates. Initially, the reaction conditions were screened with respect to different solvents and then other parameters like bases, additives and temperature were varied (Table 1). At first, the reaction was carried out in water using Cu-CuO@rGO-SiO_2 (25 mg) in the presence of K_2CO_3 (2.0 equiv.) and sodium dodecyl sulfate (SDS, 10 mol%) at 90 °C. The reaction resulted in the formation of the desired thioether, **3a** in 87% isolated yield (entry 1). The same reaction in the absence of SDS resulted in a relatively lower yield of the product (63%, entry 2). We then carried out the same reaction in the presence of EtOH, which furnished the desired product in 53% yield (entry 3). The reaction when conducted in the presence of polar aprotic solvents like DMF and CH_3CN, the desired product was obtained in 79% and 82% yields, respectively (entries 4 and 5). We performed another reaction in water in the presence of tetrabutylammonium bromide (TBAB, 10 mol%), which increased the yield of the product to 91% (entry 6). To check the role of the base, we performed the same reaction using Na_2CO_3 and KOH which resulted in 84% and 87% yield of the desired product respectively (entries 7 and 8). The reaction when conducted at room temperature gave meagre conversion even after 24 h (entry 9). While increasing the amount of the catalyst resulted in a similar conversion (92%, entry 10), reducing the catalyst loading to 15 mg per mmol of the reactant afforded the

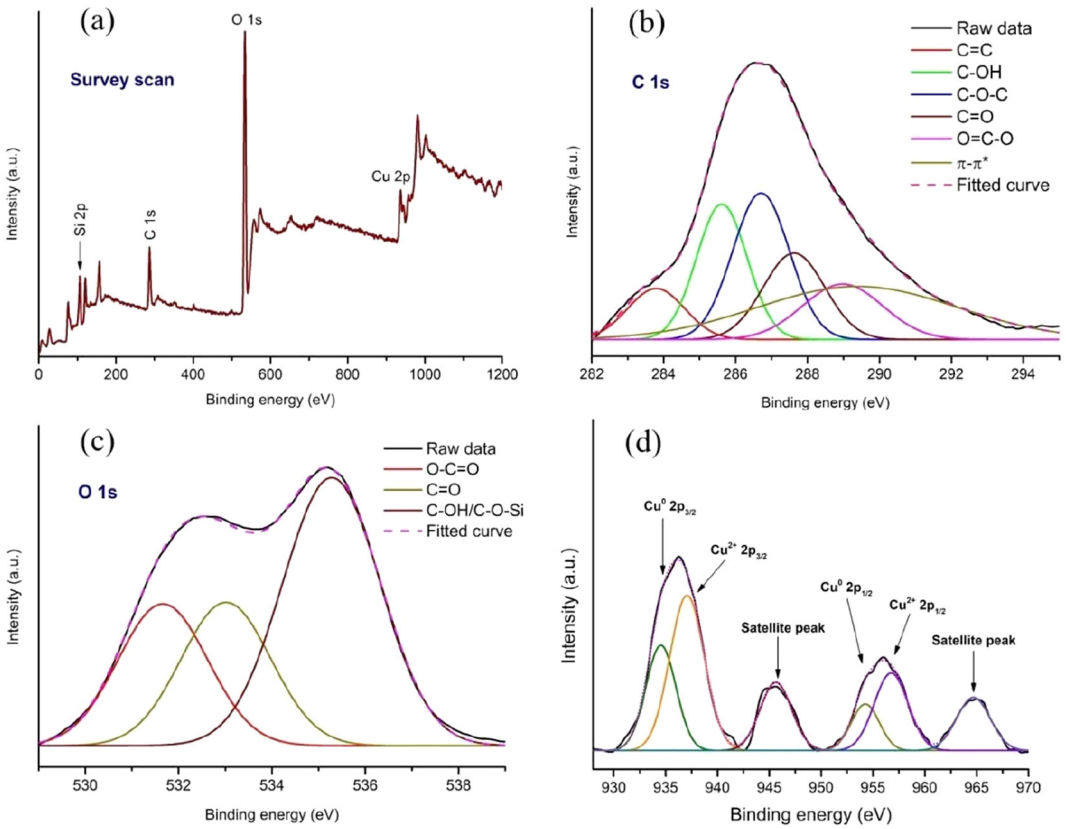

Fig. 7 XPS analysis of the Cu-CuO@rGO-SiO_2 nanocomposite. Survey scan (a), high resolution C 1s (b), high resolution O 1s (c), and high resolution Cu 2p (d).

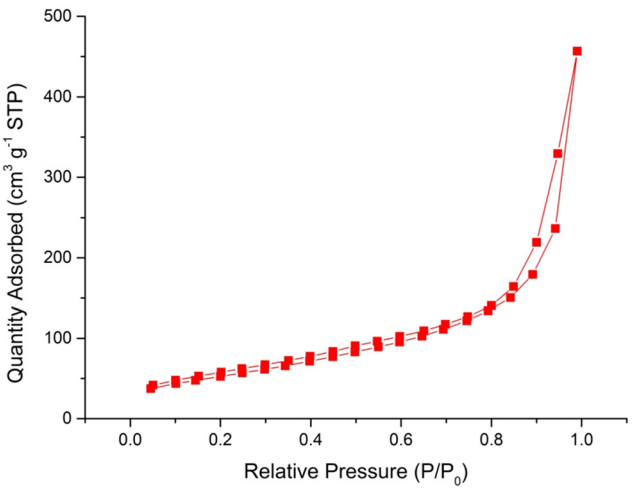

Fig. 8 BET analysis of the surface area of the Cu-CuO@rGO-SiO_2 nanocomposite.

product in a lower yield (82%, entry 11). The reaction did not proceed in the absence of the catalyst, which corroborated the active role of the catalyst during the reaction (entry 12). However, the reaction when carried out in the absence of both solvent and additive, the yield of the product reduced significantly to 54% (entry 13). We conducted one experiment without using a base, which gave a poor yield of the product (48%, entry 14). To gain more insights into the specific roles of Cu and CuO species, we prepared Cu@rGO-SiO_2 and CuO@rGO-SiO_2 catalysts following a previously reported method with minor modifications.[59] Subsequently, we carried out two separate reactions using Cu@rGO-SiO_2 and CuO@rGO-SiO_2 catalysts, which afforded the desired product in 80% and 63% yield, respectively (entries 15 and 16). The turnover number (TON) of the catalyst was found to be 35 under the optimized reaction conditions (entry 6).

With the optimized reaction conditions in hand, the substrate scope with various aryl halides and thiols was thoroughly explored (Table 2). Aryl iodides bearing electron-donating (–Me and –OMe) as well as electron-withdrawing groups (–NO_2 and –COMe) gave good to excellent yields of the corresponding thioethers (**3a–3i**). The reaction between the aryl bromide and aryl thiol gave a relatively lower yield of the corresponding thioether (**3a**, 84%). Aryl thiols bearing electron-donating (–Me and –OMe) and electron-withdrawing groups (–F) also reacted efficiently. Moreover, we carried out one reaction between 4-iodoanisole and 1-pentanethiol, which furnished the desired product (**3i**) in 80% isolated yield. Thus the presence of different functional groups and their substi-

Table 1 Optimization of the reaction conditions[a]

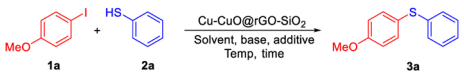

Entry	Catalyst (mg)	Solvent	Base	Additive	Temp (°C)/time (h)	Yield[b] (%)
1	25	H_2O	K_2CO_3	SDS	90/8	87
2	25	H_2O	K_2CO_3	—	90/8	63
3	25	EtOH	K_2CO_3	—	80/8	53
4	25	DMF	K_2CO_3	—	90/8	79
5	25	CH_3CN	K_2CO_3	—	80/8	82
6[c]	**25**	**H_2O**	**K_2CO_3**	**TBAB**	**90/8**	**91**
7	25	H_2O	Na_2CO_3	TBAB	90/8	84
8	25	H_2O	KOH	TBAB	90/8	87
9	25	H_2O	K_2CO_3	TBAB	r.t./24	Trace
10	35	H_2O	K_2CO_3	TBAB	90/8	92
11	15	H_2O	K_2CO_3	TBAB	90/8	82
12	—	H_2O	K_2CO_3	TBAB	90/8	No reaction
13	25	—	K_2CO_3	—	90/8	54
14	25	H_2O	—	TBAB	90/8	48
15[d]	25	H_2O	K_2CO_3	TBAB	90/8	80
16[e]	25	H_2O	K_2CO_3	TBAB	90/8	63

[a] Reaction conditions: 4-iodoanisole (1 mmol), thiophenol (1.2 mmol), base (2 mmol), solvent (2 mL) and additive (10 mol%). [b] Isolated yield after purification through column chromatography. [c] Turnover number (TON) of the catalyst is 35. [d] Reaction carried out using the Cu@rGO-SiO_2 catalyst. [e] Reaction carried out using the CuO@rGO-SiO_2 catalyst.

Table 2 Cu-CuO@rGO-SiO_2 catalyzed synthesis of thioethers[a]

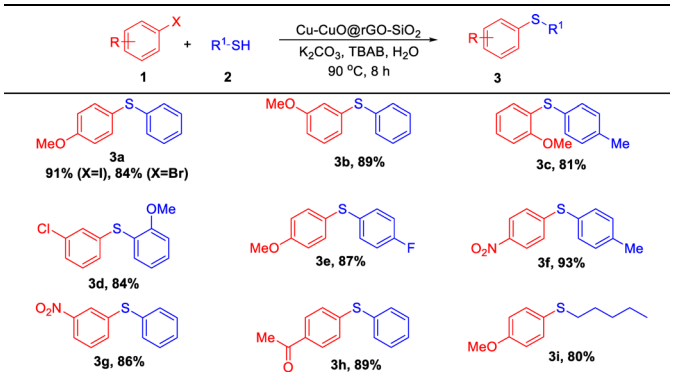

[a] Reaction conditions: **1** (1 mmol), **2** (1 mmol), Cu-CuO@rGO-SiO_2 (25 mg), K_2CO_3 (2 mmol), TBAB (10 mol%) and H_2O (2 mL) were stirred at 90 °C for 8 h.

tution pattern did not have any significant influence during the course of the reaction.

Cu-CuO@rGO-SiO_2 nanocomposite catalyzed C–O cross-coupling reaction

We next attempted the C–O cross-coupling reaction between phenols and aryl iodides using the Cu-CuO@rGO-SiO_2 nanocomposite catalyst. To optimize the reaction conditions 4-iodoanisole (**1a**, 1.0 mmol) and 4-hydroxytoluene (**4a**, 1.0 mmol) were selected as the model coupling partners. The catalytic activity of the Cu-CuO@rGO-SiO_2 nanocomposite was optimized in the presence of various solvents (DMF, DMSO, toluene, EtOH and H_2O), bases (K_2CO_3, Cs_2CO_3, KF and K_3PO_4) and ligands (2,2′-bipyridine; 1,10-phenanthroline and L-proline) at different temperatures (Table 3). The best conditions were achieved in the presence of K_3PO_4 (1 mmol) as the base and 2,2′-bipyridine (10 mol%) as the ligand in DMF at 110 °C (entry 8). The turnover number (TON) of the catalyst was determined by assessing the copper content in the nanocomposite using ICP-MS. The TON value was found to be 35 under the optimized reaction conditions (entry 8).

With the optimized reaction conditions in hand, we have studied the substrate scope with various aryl iodides, and bromides with substituted phenols (Table 4). Aryl iodides bearing electron-donating (–OMe and –Me) as well as electron-withdrawing (–NO_2 and –COMe) groups gave good to excellent yields of the corresponding diarylethers. Moreover, we observed that aryl iodides showed better response than aryl bromides in terms of yield of the products (**5b** and **5e**).

Cu-CuO@rGO-SiO_2 nanocomposite catalyzed C–N cross-coupling reaction

We next employed the ternary nanocomposite for the C–N cross-coupling reaction with aryl halides and imidazoles. The reaction was optimized by altering the solvent, base and temperature of the reaction (Table 5). Initially 4-iodotoluene (**1b**, 1 mmol) and imidazole (**6a**, 1 mmol) were chosen as the standard coupling partners. The catalytic activity of the Cu-CuO@rGO-SiO_2 nanocomposite was examined under various solvents (DMF, DMSO, H_2O, EtOH and MeCN) and bases

Table 3 Optimization of the reaction conditions[a]

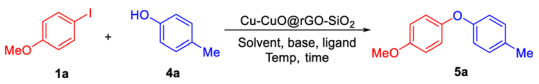

Entry	Catalyst (mg)	Solvent	Base	Ligand[b]	Temp (°C)/time (h)	Yield[c] (%)
1	25	DMF	K_2CO_3	L1	110/24	71
2	25	DMSO	K_2CO_3	L1	110/24	65
3	25	Toluene	K_2CO_3	L1	110/24	41
4	25	EtOH	K_2CO_3	L1	80/24	30
5	25	H_2O	K_2CO_3	L1	100/24	Trace
6	25	DMF	Cs_2CO_3	L1	110/24	58
7	25	DMF	KF	L1	110/24	38
8[d]	**25**	**DMF**	**K_3PO_4**	**L1**	**110/24**	**91**
9	25	DMF	K_3PO_4	L2	110/24	87
10	25	DMF	K_3PO_4	L3	110/24	40
11	25	DMF	K_3PO_4	L1	r.t./24	No reaction
12	35	DMF	K_3PO_4	L1	110/24	93
13	15	DMF	K_3PO_4	L1	110/24	79
14	—	DMF	K_3PO_4	L1	110/24	No reaction
15	25	DMF	—	L1	110/24	Trace
16	25	DMF	K_3PO_4	—	110/24	43

[a] Reaction conditions: **1a** (1.0 mmol), **4a** (1.0 mmol), base (1 mmol), ligand (10 mol%) and solvent (2 mL). [b] Ligand: L1 = 2,2′-bipyridine, L2 = 1,10-phenanthroline and L3 = L-proline. [c] Isolated yield after purification through column chromatography. [d] Turnover number (TON) value of the catalyst is 35.

Table 4 Cu-CuO@rGO-SiO_2 catalyzed synthesis of diarylethers[a]

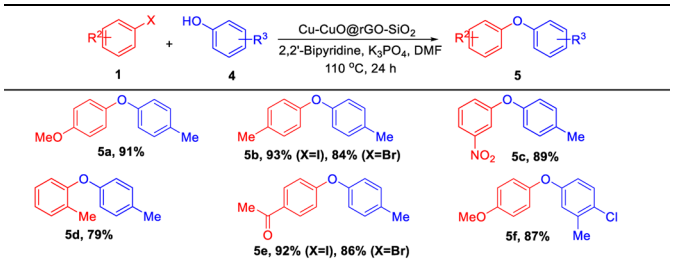

[a] Reaction conditions: **1** (1 mmol), **4** (1 mmol), Cu-CuO@rGO-SiO_2 (25 mg), K_3PO_4 (2 mmol), 2,2′-bipyridine (10 mol%) and DMF (2 mL) were stirred at 110 °C for 24 h.

Table 5 Optimization of the reaction conditions[a]

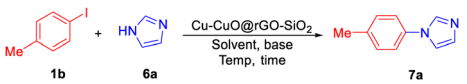

Entry	Catalyst (mg)	Solvent	Base	Temp (°C)/]time (h)	Yield[b] (%)
1	25	DMF	K_2CO_3	110/24	68
2	25	DMSO	K_2CO_3	110/24	73
3	25	H_2O	K_2CO_3	100/24	32
4	25	EtOH	K_2CO_3	80/24	39
5	25	MeCN	K_2CO_3	80/24	79
6[c]	**25**	**MeCN**	**KOH**	**80/24**	**86**
7	25	MeCN	NaOH	80/24	75
8	—	MeCN	KOH	80/24	No reaction

[a] Reaction conditions: **1b** (1 mmol), **6a** (1 mmol), base (2 mmol) and solvent (2 mL). [b] Isolated yield after purification through column chromatography. [c] Turnover number (TON) of the catalyst is 34.

(K_2CO_3, KOH and NaOH) at different temperatures. The most suitable reaction conditions were achieved in the presence of KOH (2 mmol) and MeCN at 80 °C (entry 6). Moreover, the reaction did not occur in the absence of the catalyst (entry 7) indicating the significant role of the catalytic system. The TON value of the catalyst was also determined and found to be 34 for the optimized reaction conditions (entry 6).

With the optimized reaction conditions in hand, we have explored the substrate scope with various aryl halides with imidazole and benzimidazole. The results are presented in Table 6. It was found that aryl iodides bearing both electron-donating (–Me and –OMe) and electron-withdrawing (–NO_2) groups furnished the desired products in 80–89% isolated yields. Moreover, when the reaction was carried out using a heteroaryl halide (2-bromopyridine), the corresponding product (**7g**) was obtained in 89% yield.

Mechanistic cycle of various cross coupling reactions (C–S, C–O and C–N)

The experimental results of different cross-coupling reactions clearly suggest that the reactions must occur on the heterogeneous surface *via* Cu–CuO species (Fig. 9). The combined network of carbon and silica in the catalyst surface system plays an important role in enhancing the cross-coupling process. The coupling among aryl/heteroaryl halide with the desired nucleophile (S, N, O) is highly dependent on the proximity and activation of both the coupling partners in the catalyst matrices. The as-synthesized catalytic system having a large specific surface area with a lesser oxygenated functional

Table 6 Cu-CuO@rGO-SiO_2 catalyzed C–N cross coupling reaction[a]

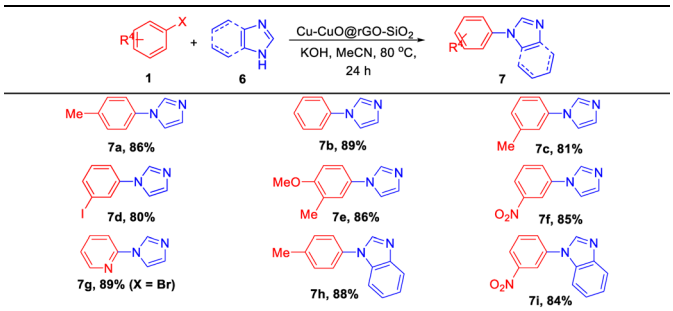

[a] Reaction conditions: **1** (1 mmol), **6** (1 mmol), Cu-CuO@rGO-SiO_2 (25 mg), KOH (2 mmol) and MeCN (2 mL) were stirred at 80 °C for 24 h.

group binds selectively to an innumerable number of aryl halide substrates. In addition, due to the acidic surface of Si–OH in the silicon network in rGO, the *in situ* generated negatively charged nucleophile becomes stable enough to couple in the presence of the metal catalyst. It is therefore proposed that the aryl halides react with the as-synthesized Cu-CuO@rGO-SiO_2 catalyst in the first step to form an intermediate **a**. In the second step, the activated nucleophile ($R–S^-$, $R–O^-$, $R–N^-$) substitutes the halide groups from intermediate **a** to form another intermediate **b**. Finally, the C–Nu bond is formed by reductive elimination from intermediate **b**. The unique synergism between Cu(0) and CuO species in the cross-coupling reactions have been experimentally supported by employing Cu@rGO-SiO_2 and CuO@rGO-SiO_2 catalysts separately in two C–S cross-coupling reactions. The first reaction using Cu@rGO-SiO_2 resulted in the formation of diaryl sulfide (**3a**) in 80% yield (Table 1, entry 15), while the second reaction using CuO@rGO-SiO_2 afforded **3a** in 63% yield (Table 1, entry 16). In contrast, the new ternary catalytic system (Cu-CuO@rGO-SiO_2), when employed in the same reaction, furnished the desired product (**3a**) in a relatively higher yield (91%, Table 1, entry 6). Based on these observations, we presumed a synergistic interaction between different copper species. Moreover, the unique synergism of different copper species and facile charge transfer from the metal ions towards the rGO-SiO_2 surface apparently facilitated smooth oxidative addition and reductive elimination processes, which in turn afforded enhanced catalytic performance in multifarious cross-coupling reactions (Fig. 9).

Recyclability of the Cu-CuO@rGO-SiO_2 nanocomposite

We have performed the recyclability of the Cu-CuO@rGO-SiO_2 catalyst in the C–S cross-coupling reaction under the optimized

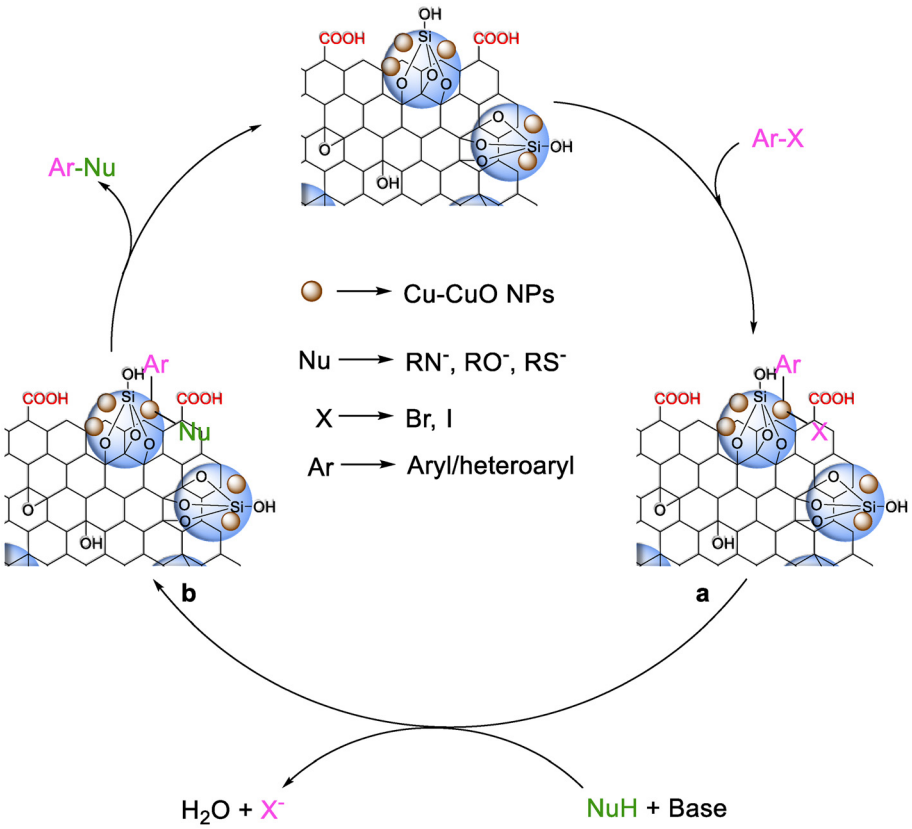

Fig. 9 Mechanistic cycle of Cu-CuO@rGO-SiO_2 catalyzed various cross coupling reactions.

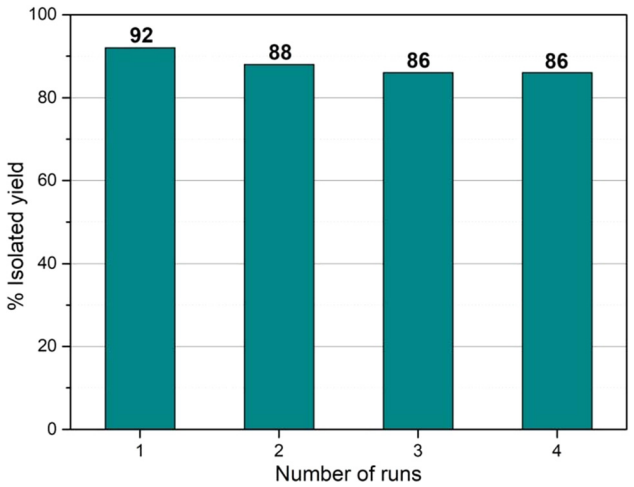

Fig. 10 Recyclability of the Cu-CuO@rGO-SiO_2 nanocomposite in the C–S cross-coupling reaction.

conditions (Table 1, entry 5). After the first run, the catalyst was separated from the reaction mixture by simple filtration, washed with ethyl acetate (3 × 5 mL) and dried under vacuum for 24 h. It was then re-used for the next catalytic run. The catalyst was re-used for four consecutive runs without any significant drop in the yield of the product (Fig. 10). Moreover, we characterized the catalyst after the third run using FT-IR and did not observe any significant change in the characteristic peaks (Fig. S4.I in the ESI†). The Raman spectra also indicated no changes in the catalyst after the third run (Fig. S4.II in the ESI†). The morphology of the recovered catalyst (after the third run) was also studied by SEM, SEM-EDS, HRTEM and PXRD analyses. The SEM image of the catalyst after a catalytic run showed no substantial change in the surface of the nanocomposite. In the SEM-EDS image, the wt% of copper did not decrease significantly in the recovered catalyst which suggested the robustness of the nanocomposite (Fig. S4.III in the ESI†). The HRTEM images clearly showed the presence of uniformly distributed Cu(0) and CuO species on the rGO-SiO_2 surface (Fig. S4.IV in the ESI†). Additionally, the average size of the Cu (0) and CuO species remained in the range of 5–15 nm which confirmed that the copper species did not aggregate after the reaction, thereby exhibiting catalytic efficiency even after the third run. Moreover, the XRD patterns of Cu-CuO@rGO-SiO_2 after the third run showed diffraction peaks at $2\theta \sim 43.4°$ (111) and 50.5° (200) for Cu(0) and at $2\theta \sim 77.9°$ (222) for CuO species (Fig. S4.V in the ESI†).

Conclusions

In conclusion, a novel, suitably fabricated Cu/CuO supported rGO-SiO_2 nanocomposite has been synthesized, characterized and demonstrated as a sustainable and multi-tasking heterogeneous catalyst for C–X (X = S, O, N) cross-coupling reactions. To the best of our knowledge, this is the first example of a single heterogeneous catalyst that can efficiently perform in different coupling reactions. A broad catalytic performance has been presumably possible due to the synergistic interaction between different copper species having spread over the multi-layered hybrid assembly of rGO and silica. Moreover, the combination of rGO and ordered silica channels might prevent the aggregation of copper species thereby offering enhanced catalytic activity and proved to be a robust catalyst. As a result, facile charge transfer from the metal ions towards the rGO-SiO_2 surface matrices is likely to facilitate the oxidative addition and reductive elimination processes, as also discussed in the plausible mechanistic routes of coupling reactions. We believe that easy preparation of the ternary nanocomposite and such a multi-tasking catalytic role of a single catalytic combination could pave the way to develop new catalysts to be effective for a wider variety of organic reactions.

Author contributions

P. C. and S. G. synthesized the nanocomposite catalyst. P. C. analyzed the catalyst, performed the cross-coupling experiments and wrote the draft manuscript. K. B. and B. B. conceived the research, supervised and revised the manuscript. All authors have discussed the results and approved the final version of the manuscript.

Conflicts of interest

There are no conflicts of interest to declare.

Acknowledgements

We thank the University of North Bengal for the infrastructural support. S. G. is thankful to his institution, Raiganj Surendranath Mahavidyalaya, Raiganj, Uttar Dinajpur, West Bengal, India. The authors also thank MNIT-MRC, Jaipur, India for the BET analyzer facility.

References

1 I. P. Beletskaya and V. P. Ananikov, *Chem. Rev.*, 2022, **122**, 16110–16293.
2 S. Vásquez-Céspedes, R. C. Betori, M. A. Cismesia, J. K. Kirsch and Q. Yang, *Org. Process Res. Dev.*, 2021, **25**, 740–753.
3 J. Lou, Q. Wang, P. Wu, H. Wang, Y.-G. Zhou and Z. Yu, *Chem. Soc. Rev.*, 2020, **49**, 4307–4359.
4 P. Devendar, R.-Y. Qu, W.-M. Kang, B. He and G.-F. Yang, *J. Agric. Food Chem.*, 2018, **66**, 8914–8934.
5 P. Ruiz-Castillo and S. L. Buchwald, *Chem. Rev.*, 2016, **116**, 12564–12649.
6 J. He, M. Wasa, K. S. Chan, Q. Shao and J.-Q. Yu, *Chem. Rev.*, 2017, **117**, 8754–8786.

7 K. Hong, M. Sajjadi, J. M. Suh, K. Zhang, M. Nasrollahzadeh, H. W. Jang, R. S. Varma and M. Shokouhimehr, *ACS Appl. Nano Mater.*, 2020, **3**, 2070–2103.
8 Á. Molnár, *Chem. Rev.*, 2011, **111**, 2251–2320.
9 D. Sun, M. Xu, Y. Jiang, J. Long and Z. Li, *Small Methods*, 2018, **2**, 1800164.
10 L. Wang, R. Sa, Y. Wei, X. Ma, C. Lu, H. Huang, E. Fron, M. Liu, W. Wang, S. Huang, J. Hofkens, M. B. J. Roeffaers, Y.-j. Wang, J. Wang, J. Long, X. Fu and R. Yuan, *Angew. Chem., Int. Ed.*, 2022, **61**, e202204561.
11 L. Meng, Z. Chen, Z. Ma, S. He, Y. Hou, H.-H. Li, R. Yuan, X.-H. Huang, X. Wang, X. Wang and J. Long, *Energy Environ. Sci.*, 2018, **11**, 294–298.
12 Y. Wang, H. Li, Q. Lin, J. Zhao, X. Fang, N. Wen, Z. Zhang, Z. Ding, R. Yuan, X.-H. Huang and J. Long, *ACS Catal.*, 2023, **13**, 15493–15504.
13 Q. Lin, S. Tan, J. Zhao, X. Fang, Y. Wang, N. Wen, Z. Zhang, Z. Ding, R. Yuan, G. Yan, S. Jin and J. Long, *Small*, 2024, **20**, 2304776.
14 Q. Gu, Q. Jia, J. Long and Z. Gao, *ChemCatChem*, 2019, **11**, 669–683.
15 M. B. Gawande, A. Goswami, F.-X. Felpin, T. Asefa, X. Huang, R. Silva, X. Zou, R. Zboril and R. S. Varma, *Chem. Rev.*, 2016, **116**, 3722–3811.
16 S. Thapa, B. Shrestha, S. K. Gurung and R. Giri, *Org. Biomol. Chem.*, 2015, **13**, 4816–4827.
17 T. Aneeja, M. Neetha, C. Afsina and G. Anilkumar, *RSC Adv.*, 2020, **10**, 34429–34458.
18 P. J. A. Joseph and S. Priyadarshini, *Org. Process Res. Dev.*, 2017, **21**, 1889–1924.
19 G. Ma, O. A. Syzgantseva, Y. Huang, D. Stoian, J. Zhang, S. Yang, W. Luo, M. Jiang, S. Li and C. Chen, *Nat. Commun.*, 2023, **14**, 501.
20 B. Ma, C. Kong, J. Lv, X. Zhang, S. Yang, T. Yang and Z. Yang, *Adv. Mater. Interfaces*, 2020, **7**, 1901643.
21 D. Chakraborty, S. Nandi, D. Mullangi, S. Haldar, C. P. Vinod and R. Vaidhyanathan, *ACS Appl. Mater. Interfaces*, 2019, **11**, 15670–15679.
22 S. Kapoor, A. Sheoran, M. Riyaz, J. Agarwal, N. Goel and S. Singhal, *J. Catal.*, 2020, **381**, 329–346.
23 P. C. Caldas, J. M. R. Gallo, A. Lopez-Castillo, D. Zanchet and J. M. C. Bueno, *ACS Catal.*, 2017, **7**, 2419–2424.
24 A. A. Mashentseva, M. Barsbay, M. V. Zdorovets, D. A. Zheltov and O. Güven, *Nanomaterials*, 2020, **10**, 1552.
25 Z. Jin, C. Liu, K. Qi and X. Cui, *Sci. Rep.*, 2017, **7**, 39695.
26 G. Xu, J. Huang, X. Li, Q. Chen, Y. Xie, Z. Liu, K. Kajiyoshi, L. Wu, L. Cao and L. Feng, *Catalysts*, 2023, **13**, 255.
27 A. Wang, J. Guan, L. Zhang, H. Wang, G. Ma, G. Fan, W. Tang, N. Han and Y. Chen, *J. Phys. Chem. C*, 2022, **126**, 317–325.
28 B. Wei, N. Yang, F. Pang and J. Ge, *J. Phys. Chem. C*, 2018, **122**, 19524–19531.
29 J. Kanarat, T. Bunchuay, W. Klysubun and J. Tantirungrotechai, *ChemCatChem*, 2021, **13**, 4833–4840.
30 A. K. Kar and R. Srivastava, *Inorg. Chem. Front.*, 2019, **6**, 576–589.
31 M. Karimzadeh, K. Niknam, N. Manouchehri and D. Tarokh, *RSC Adv.*, 2018, **8**, 25785–25793.
32 A. K. Sasmal, S. Dutta and T. Pal, *Dalton Trans.*, 2016, **45**, 3139–3150.
33 R. F. Gomes, L. A. Cavaca, J. M. Goncalves, R. Ramos, A. F. Peixoto, B. I. Arias-Serrano and C. A. Afonso, *ACS Sustainable Chem. Eng.*, 2021, **9**, 16038–16043.
34 J. Xu, Y. Qin, H. Wang, F. Guo and J. Xie, *New J. Chem.*, 2020, **44**, 817–831.
35 D. Y. Zheng, R. Bai, M. Li and Y. Gu, *ChemCatChem*, 2022, **14**, e202200235.
36 Y. Ma, X. Han, S. Xu, Z. Wang, W. Li, I. Da Silva, S. Chansai, D. Lee, Y. Zou and M. Nikiel, *J. Am. Chem. Soc.*, 2021, **143**, 10977–10985.
37 J. Martínez-Laguna, A. Caballero and P. J. Pérez, *Adv. Synth. Catal.*, 2021, **363**, 1740–1755.
38 O. Mohammadi, M. Golestanzadeh and M. Abdouss, *New J. Chem.*, 2017, **41**, 11471–11497.
39 M.-H. Sun, S.-Z. Huang, L.-H. Chen, Y. Li, X.-Y. Yang, Z.-Y. Yuan and B.-L. Su, *Chem. Soc. Rev.*, 2016, **45**, 3479–3563.
40 M. A. Pirlar, Y. Honarmand, M. R. Mirghaed, S. M. S. Movahed and R. Karimzadeh, *ACS Appl. Nano Mater.*, 2020, **3**, 2123–2128.
41 M. Nallal, K. H. Park, S. Park, J. Kim, S. Shenoy, C. Chuaicham, K. Sasaki and K. Sekar, *ACS Appl. Nano Mater.*, 2022, **5**, 17271–17280.
42 A. Gupta, R. Jamatia, R. A. Patil, Y.-R. Ma and A. K. Pal, *ACS Omega*, 2018, **3**, 7288–7299.
43 J. Li, H. Zeng, Z. Zeng, Y. Zeng and T. Xie, *ACS Biomater. Sci. Eng.*, 2021, **7**, 5363–5396.
44 F. Hu, M. Patel, F. Luo, C. Flach, R. Mendelsohn, E. Garfunkel, H. He and M. Szostak, *J. Am. Chem. Soc.*, 2015, **137**, 14473–14480.
45 L. Shang, T. Bian, B. Zhang, D. Zhang, L.-Z. Wu, C.-H. Tung, Y. Yin and T. Zhang, *Angew. Chem., Int. Ed.*, 2014, **53**, 250–254.
46 X. Yu and C. T. Williams, *Catal. Sci. Technol.*, 2022, **12**, 5765–5794.
47 C. Damian, M. Necolau, I. Neblea, E. Vasile and H. Iovu, *Appl. Surf. Sci.*, 2020, **507**, 145046.
48 C. Sarkar, S. Pendem, A. Shrotri, D. Q. Dao, P. P. T. Mai, T. N. Ngoc, D. R. Chandaka, T. V. Rao, Q. T. Trinh and M. P. Sherburne, *ACS Appl. Mater. Interfaces*, 2019, **11**, 11722–11735.
49 P. Choudhury, S. Chattopadhyay, G. De and B. Basu, *Mater. Adv.*, 2021, **2**, 3042–3050.
50 W. L. Zhang and H. J. Choi, *Langmuir*, 2012, **28**, 7055–7062.
51 M. Aunkor, I. Mahbubul, R. Saidur and H. Metselaar, *RSC Adv.*, 2016, **6**, 27807–27828.
52 A. Abdelkhalek, M. A. El-Latif, H. Ibrahim, H. Hamad and M. Showman, *Sci. Rep.*, 2022, **12**, 7060.
53 K. G. Lee, R. Wi, M. Imran, T. J. Park, J. Lee, S. Y. Lee and D. H. Kim, *ACS Nano*, 2010, **4**, 3933–3942.

54 D. C. T. Nguyen, K. Y. Cho and W.-C. Oh, *RSC Adv.*, 2017, **7**, 29284–29294.
55 F. Yang, B. Zhang, S. Dong, Y. Tang, L. Hou, Z. Chen, Z. Li, W. Yang, C. Xu and M. Wang, *Appl. Surf. Sci.*, 2018, **452**, 11–18.
56 H. Zarrin, D. Higgins, Y. Jun, Z. Chen and M. Fowler, *J. Phys. Chem. C*, 2011, **115**, 20774–20781.
57 A. Yin, X. Guo, W.-L. Dai and K. Fan, *J. Phys. Chem. C*, 2009, **113**, 11003–11013.
58 V. H. Luan, H. N. Tien, L. T. Hoa, N. T. M. Hien, E.-S. Oh, J. Chung, E. J. Kim, W. M. Choi, B.-S. Kong and S. H. Hur, *J. Mater. Chem. A*, 2013, **1**, 208–211.
59 M. E. Shabestari, O. Martín, D. Díaz-García, S. Gómez-Ruiz, V. J. Gonzalez and J. Baselga, *Carbon*, 2020, **161**, 7–16.